Meng *et al. Energy Mater.* **2025**, *5*, 500142
DOI: 10.20517/energymater.2025.113

Energy Materials

Communication

Open Access

Check for updates

Fe^{3+}-driven tunnel engineering for stabilizing metastable ramsdellite MnO_2 in high-performance zinc-ion batteries

Yutong Meng[1], Yangfan Li[1], Hang Xiao[1], Xiang Wang[1], Zhiwen Wang[1], Fan Zhang[2,*], Wenqing Ma[3], Da Xiong[1], Zisheng Xiao[1,*], Jiang Yin[1], Zhiye Yuan[4], Tong Zhou[4], Lishan Yang[1,*], Changhui Liu[5], Xiongwei Wu[1]

[1]Key Laboratory of Chemical Biology & Traditional Chinese Medicine Research (Ministry of Education of China), National and Local Joint Engineering Laboratory for New Petrochemical Materials and Fine Utilization of Resources, Key Laboratory of the Assembly and Application of Organic Functional Molecules of Hunan Province, Key Laboratory of Light Energy Conversion Materials of Hunan Province, Hunan Normal University, Changsha 410081, Hunan, China.
[2]College of Chemistry and Chemical Engineering, Central South University, Changsha 410083, Hunan, China.
[3]Institute for Advanced Interdisciplinary Research (iAIR), Collaborative Innovation Center of Technology and Equipment for Biological Diagnosis and Therapy in Universities of Shandong, School of Chemistry and Chemical Engineering, University of Jinan, Jinan 250022, Shandong, China.
[4]Xiangtan Electrochemical Technology Co., Ltd, Xiangtan 411100, Hunan, China.
[5]College of Chemistry and Chemical Engineering, Hunan Institute of Science and Technology, Yueyang, 414006, Hunan, China.

[*]**Correspondence to:** Prof. Lishan Yang and Dr. Zisheng Xiao, College of Chemistry and Chemical Engineering, Hunan Normal University, No.036 Lushan Road, Changsha 410081, Hunan, China. E-mail: lsyang@hunnu.edu.cn; zishengxiao@hunnu.edu.cn; Dr. Fan Zhang, College of Chemistry and Chemical Engineering, Central South University, No.932 South Lushan Road, Changsha 410083, Hunan, China. E-mail: 242301028@csu.edu.cn.

How to cite this article: Meng, Y.; Li, Y.; Xiao, H.; Wang, X.; Wang, Z.; Zhang, F.; Ma, W.; Xiong, D.; Xiao, Z.; Yin, J.; Yuan, Z.; Zhou, T.; Yang, L.; Liu, C.; Wu, X. Fe^{3+}-driven tunnel engineering for stabilizing metastable ramsdellite MnO_2 in high-performance zinc-ion batteries. *Energy Mater.* **2025**, *5*, 500142. https://dx.doi.org/10.20517/energymater.2025.113

Received: 10 Jul 2025 **First Decision:** 24 Jul 2025 **Revised:** 30 Jul 2025 **Accepted:** 13 Aug 2025 **Published:** 28 Aug 2025

Academic Editor: Bin Wang **Copy Editor:** Ping Zhang **Production Editor:** Ping Zhang

Abstract

Ramsdellite MnO_2 (*R*-MnO_2), with its expanded (1 × 2) tunnels, offers superior Zn^{2+} diffusion kinetics for aqueous zinc-ion batteries but suffers from metastability-induced phase collapse. Herein, Fe^{3+} doping is demonstrated as a critical strategy to thermodynamically stabilize *R*-MnO_2 while optimizing its electrochemical functionality. Through a synergistic H^+/Fe^{3+} hydrothermal process, spent $ZnMn_2O_4$ from alkaline batteries is converted into orthorhombic *R*-$Fe_xMn_{1-x}O_2$ nanocrystals. Fe^{3+} incorporation enlarges the tunnel structure, reduces surface energy, and mitigates Jahn-Teller distortion by increasing the Mn^{4+}/Mn^{3+} ratio. This yields a high specific surface area, enhanced ion diffusion kinetics, and exceptional cycling stability. The *R*-$Fe_xMn_{1-x}O_2$ cathode achieves a 286.8 mAh g^{-1} capacity at 0.1 A g^{-1}, outperforming β-MnO_2 (30.9 mAh g^{-1} at 1.5 A g^{-1}). This work establishes Fe^{3+} doping as an essential

© The Author(s) 2025. **Open Access** This article is licensed under a Creative Commons Attribution 4.0 International License (https://creativecommons.org/licenses/by/4.0/), which permits unrestricted use, sharing, adaptation, distribution and reproduction in any medium or format, for any purpose, even commercially, as long as you give appropriate credit to the original author(s) and the source, provide a link to the Creative Commons license, and indicate if changes were made.

mechanism for stabilizing high-performance metastable cathodes, enabling sustainable upcycling of battery waste.

Keywords: Ramsdellite MnO_2, zinc-ion batteries, energy density, chemical and electrochemical stability

INTRODUCTION

Aqueous zinc-ion batteries (AZIBs) have attracted significant attention due to their high safety, low cost, and environmentally friendly characteristics[1-3]. Among previously reported cathode materials, Mn-based oxides have become promising cathode materials for AZIBs due to their advantages in safety and high theoretical capacity. Mn-based materials from spent alkaline batteries (SABs) share chemical homology with AZIB cathodes, enabling resource regeneration from spent batteries into high-performance AZIBs[4,5]. On the other hand, the casual discarding of SABs inevitably leads to the leakage of heavy metals such as zinc (Zn) and manganese (Mn), posing potential threats to the ecological balance and human health, thereby making the recycling and safe disposal of SABs imperative[6].

Manganese dioxide (MnO_2) exhibits various phases in aqueous environments, including β-MnO_2, α-MnO_2, R-MnO_2 (ramsdellite-MnO_2), δ-MnO_2, λ-MnO_2, and γ-MnO_2. While β-MnO_2 demonstrates phase stability, it is limited by its (1 × 1) narrow tunnel structure; conversely, R-MnO_2 with (1 × 2) expanded tunnels significantly improves Zn^{2+} diffusion kinetics[7-9]. Recently, our group investigated the recycling and synthesis of β-MnO_2 from SABs through hydrochloric acid hydrothermal treatment[10]. Previous studies show that highly reactive R-MnO_2 forms initially during hydrothermal processing, but metastable R-MnO_2 transforms rapidly into β-MnO_2 with longer treatment or at high temperatures[11]. β-MnO_2 hinders H^+/Zn^{2+} extraction/insertion due to its narrow tunnels[12]. In contrast, (1 × 2) tunnels in R-MnO_2 enhance ion insertion kinetics[13]. Huang *et al.* synthesized an R-MnO_2-based composite material with supercapacitor characteristics and excellent electrochemical performance[14]. Chen *et al.* prepared R-MnO_2 through the low-valent ion doping; the material exhibits high oxygen vacancy concentration, further improving the electrical conductivity and reactivity[15]. Nevertheless, traditional synthesis methods face challenges in producing stable R-MnO_2, necessitating controllable and convenient strategies for its preparation[16,17].

Meanwhile, challenges remain; lattice collapse of metastable phases (e.g., R-MnO_2) during ion insertion causes pulverization of cathode materials. Over the years, much research has employed multidimensional regulation strategies, including ionic doping, surface engineering, and defect engineering, to optimize the physicochemical properties of materials[18]. Pan *et al.* synthesized Fe-MnO/C via annealing to achieve an MnO crystal structure and demonstrated that Mn-O-Fe bond formation promotes charge transfer kinetics while mitigating structural collapse, thereby synergistically improving rate capability and cycling stability[19]. Zhong *et al.* showed that iron doping effectively mitigates the Jahn-Teller effect, stabilizes lattice water, and prevents lattice collapse, thus regulating the layered structure in AZIBs[20]. Although ionic doping is widely utilized to stabilize MnO_2, the stabilization of metastable phases during synthesis remains underexplored[21,22].

Herein, we demonstrate that Fe^{3+} doping acts as a dual-function regulator by thermodynamically stabilizing R-MnO_2 through reduced surface energy and enlarged (1 × 2) tunnels, while kinetically enhancing Zn^{2+} diffusion via optimized Mn^{4+}/Mn^{3+} ratios that suppress Jahn-Teller effects. Through a synergistic H^+/Fe^{3+} hydrothermal process, spent $ZnMn_2O_4$ waste is successfully converted into stable R-$Fe_xMn_{1-x}O_2$ nanocrystals, achieving retention of the metastable R-phase, a high surface area of 218 $m^2\ g^{-1}$, and low charge-transfer resistance. Electrochemical performance reaches 286.8 mAh g^{-1} at 0.1 A g^{-1} with 88.9% capacity retention after 1000 cycles. This study establishes Fe^{3+} doping as a universal design principle for metastable functional

materials, offering simultaneous advancements in AZIB cathode engineering and sustainable battery upcycling.

EXPERIMENTAL

Materials

The materials used in this study include Nanford alkaline batteries (spent battery, LR6-2B/1.5V), potassium hydroxide (KOH, AR), hydrochloric acid (HCl, AR), Sulfuric acid (H_2SO_4, AR, 98 wt.%), N-methyl pyrrolidone (NMP, AR), and polyvinylidene fluoride (PVDF, AR).

Preparation of materials from spent alkaline batteries

Used Nanford alkaline batteries were further discharged to 0.8 V using a Neware Battery Test System (CT-4000). The discharged batteries were manually disassembled to collect cathode materials for further processing. The cathode powder was stirred in 0.1 M KOH solution for over 30 minutes to remove residual adhesives and alkaline compounds. The mixture was filtered and sequentially washed with 0.01 M H_2SO_4 solution, deionized (DI) water, and ethanol. The resulting precipitate was dried under vacuum at 60 °C, yielding brown-black Spent Materials (SABs).

Synthesis of β-MnO_2 and R-$Fe_xMn_{1-x}O_2$

Firstly, 0.9 g of SABs powder was dispersed in 66 mL of DI water. Then, 4 mL of concentrated hydrochloric acid (AR, 37 wt.%) was added dropwise. Subsequently, 0.2g $Fe_2(SO_4)_3$ was added under continuous stirring at 20 °C for 30 min. The mixture was then transferred to a 100 mL hydrothermal reactor and reacted at 140 °C for 12 h. The product was washed with DI water and dried in a vacuum oven at 60 °C to obtain *R*-$Fe_xMn_{1-x}O_2$. When $Fe_2(SO_4)_3$ was omitted during stirring, *β*-MnO_2 was obtained.

Characterizations

The materials were further characterized using an X-ray diffraction (XRD, Cu Kα, Bruker D8 Advanced, λ = 1.5481 Å) to obtain their structural information. The morphology and microstructure were examined using Scanning Electron Microscopy (SEM, FEI Quanta FEG 250) and Transmission Electron Microscopy (TEM, JEOL 2100). The selective area electron diffraction (SAED) patterns were employed to examine the polycrystalline nature of the materials. The surface elemental properties of the samples were analyzed using an X-ray Photoelectron Spectrometer (XPS, Thermo Fisher Scientific K-Alpha) with an Al Kα X-ray excitation source. The N_2 adsorption/desorption isotherm was measured using ASAP 2460 at 77 K, and the specific surface area was determined using the Brunauer-Emmett-Teller (BET) method.

Electrochemical measurement

The active materials (*β*-MnO_2 and *R*-$Fe_xMn_{1-x}O_2$), carbon black, and PVDF were uniformly mixed at a 7:2:1 mass ratio. The resulting slurry was coated onto stainless steel foil with mass loading of 0.8~1.2 mg cm^{-2} and vacuum-dried. The 2032 button cells were assembled using zinc foil anode and glass fiber filter (Whatman GF/D grade) as a separator. The electrolyte was a mixed solution of $ZnSO_4$ (3 M) and $MnSO_4$ (0.05 M). The electrochemical performance was evaluated using a Neware Battery Test System (CT-3008). Cyclic voltammetry (CV) was conducted on a CHI 760E electrochemical station, while electrochemical impedance spectroscopy (EIS) was recorded on a DH7000D electrochemical station.

Computational details

In order to study the mechanism of the reconstruction process, density functional theory (DFT) calculations were used to determine the surface energies of the exposed crystal surfaces *R*-$Fe_xMn_{1-x}O_2$ (210), *β*-MnO_2 (110) and *R*-MnO_2 (210) to evaluate the stability differences of various crystalline phases of MnO_2. We established *R*-$Fe_xMn_{1-x}O_2$, *R*-MnO_2 and *β*-MnO_2 cluster models using the commercially available

software, Materials Studio 2020. The Castep module was employed to perform the geometry optimization step and the corresponding calculation program of the models. The smooth part of the wave function was expanded and the kinetic energy cut-off was 500 eV. The relaxation convergence criteria for structural optimization were a maximum displacement of 1.0×10^{-3} Å and a maximum force of 0.03 eV $Å^{-1}$.

RESULT AND DISCUSSION

R-$Fe_xMn_{1-x}O_2$ was synthesized via a pretreatment of SABs (sequential cleaning with mixed alkali solutions and acid solutions) followed by a 12 h hydrothermal reaction at 140 °C co-induced by H^+ and Fe^{3+}, while *β*-MnO_2 was prepared identically without the addiction of Fe^{3+} [Figure 1A]. SEM images and XRD patterns [Figure 1B-D and Supplementary Figures 1-4] reveal the overall morphology of the original SABs and Mn-based materials. *β*-MnO_2 exhibits a regular granular structure, while *R*-$Fe_xMn_{1-x}O_2$ displays irregular shapes with numerous adhered and agglomerated small particles. XRD analysis revealed that [Figure 1C] all the diffraction peaks of *R*-$Fe_xMn_{1-x}O_2$ correspond to *R*-MnO_2 (JCPDS #42-1316), demonstrating the stability of the *R*-MnO_2 structure upon Fe^{3+} doping. In contrast, *β*-MnO_2 was identified as rutile type (JCPDS #24-0735). Although *R*-MnO_2 is generally metastable, Fe^{3+} doping stabilized the main *R*-MnO_2 phase in *R*-$Fe_xMn_{1-x}O_2$ using this synthesis method. To validate the hydrothermal regeneration pathway and the phase transformation, comprehensive materials characterization was conducted. Combined with the material source and characterization results in Supplementary Figure 2, we confirmed the presence of impurities including Zn, C, and organics in the raw materials. During pretreatment steps, Zn and organics were effectively removed, while trace residual organics underwent carbonization during the hydrothermal process, resulting in conductive carbon that does not compromise material performance. BET surface area analysis [Figure 1E, Supplementary Figure 1C and D] demonstrated a substantial increase in specific surface area (from 78.78 $m^2 g^{-1}$ to 218.01 $m^2 g^{-1}$) and higher mesopore volume for *R*-$Fe_xMn_{1-x}O_2$ compared to *β*-MnO_2. Combined with Rietveld refinement of XRD patterns, the breaking of the long-range crystal order reduced particle size, enhanced specific surface area, and enlarged pore volume of *R*-$Fe_xMn_{1-x}O_2$, establishing abundant active sites for H^+/Zn^{2+} extraction/insertion.

High-resolution XPS analysis of the Fe 2p in *R*-$Fe_xMn_{1-x}O_2$ revealed a characteristic spin-orbit splitting energy of 13.9 eV between Fe $2p_{1/2}$ and Fe $2p_{3/2}$ peaks, confirming iron predominantly exists as Fe^{3+} [Figure 1F][23]. Through Fe^{3+} doping, the Mn 2p spectra exhibited two peaks at 642.28 eV and 653.68 eV, which correspond to the characteristic peaks of Mn^{4+} in MnO_2[24]. Meanwhile, peak area analysis revealed *R*-$Fe_xMn_{1-x}O_2$ had a higher Mn^{4+} content (75%) than *β*-MnO_2 (60%), which is anticipated to effectively mitigate Jahn-Teller distortion, reduce Mn^{3+} disproportionation, and enhance conductivity [Supplementary Figures 5 and 6]. The O 1s spectra indicated greater O vacancy concentration in *R*-$Fe_xMn_{1-x}O_2$, facilitating rapid electron transfer. As potent defects, these oxygen vacancies significantly disrupt the lattice and inhibit crystal growth, which also contributed to enhanced nanoscale refinement of the material[25]. DFT calculations [Figure 1G and Supplementary Figure 7] demonstrated that Fe^{3+} doping reduces surface energy (favoring the formation of *R*-$Fe_xMn_{1-x}O_2$), enhances the surface thermodynamic stability of *R*-MnO_2, significantly releases lattice stress, modifies the anisotropy of crystal growth and improves ion transport kinetics.

TEM analysis provided detailed elucidation of the material's morphological characteristics. Figure 2A and B corroborated the morphological features observed by SEM. Compared with *β*-MnO_2 [Supplementary Figure 8]; the particle dimensions of *R*-$Fe_xMn_{1-x}O_2$ were significantly reduced, consistent with the BET surface area analysis results. SAED and High-Resolution Transmission Electron Microscopy (HRTEM) patterns verified the polycrystalline nature of *R*-$Fe_xMn_{1-x}O_2$. SAED exhibited well-defined diffraction spots corresponding to the characteristic *R*-MnO_2 (020) and (210) planes, confirming complete phase transformation to *R*-MnO_2

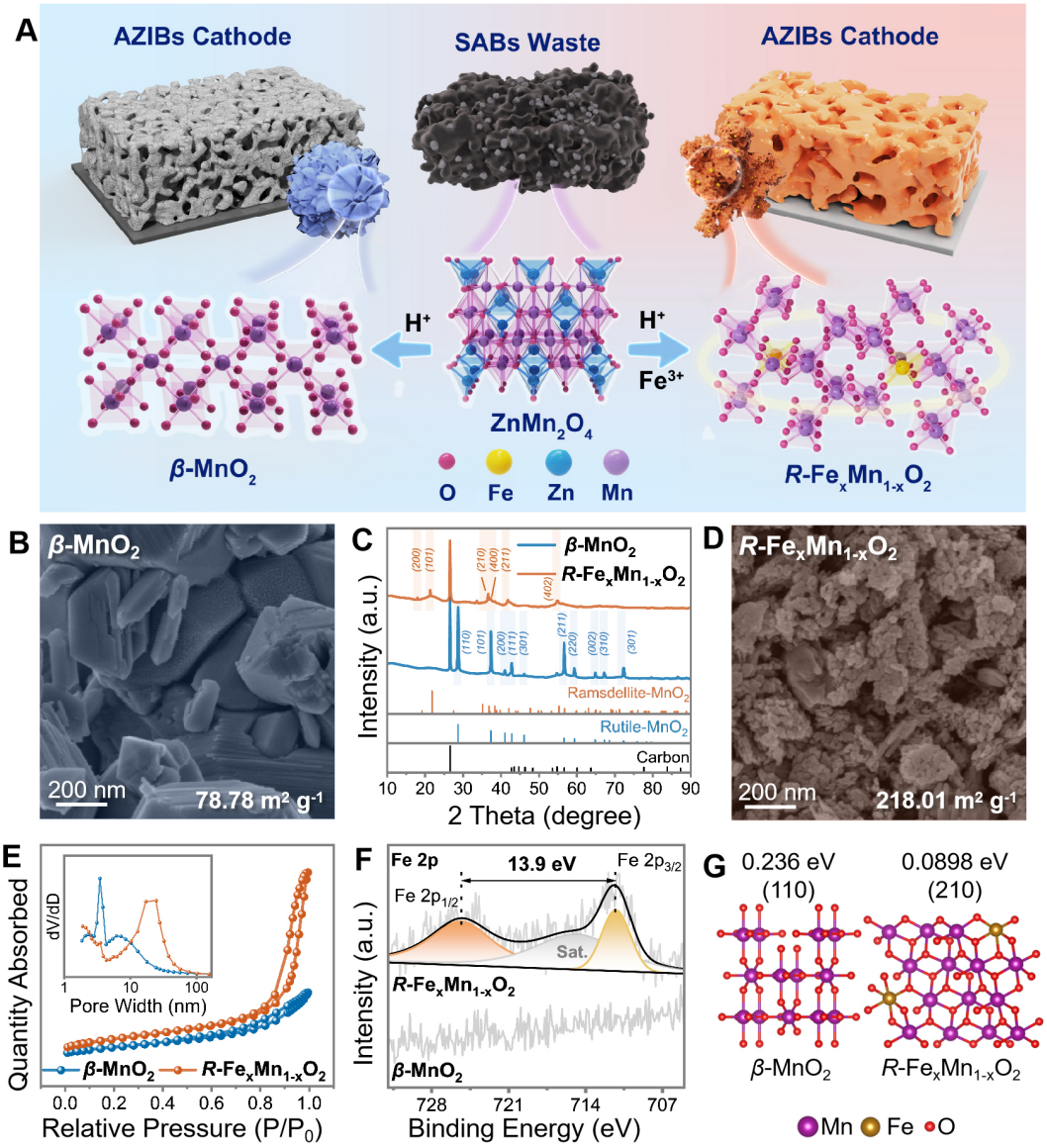


Figure 1. (A) Schematic illustration of the phase evolutions from SABs to β-MnO_2 and R-$Fe_xMn_{1-x}O_2$; SEM image and BET surface area of (B) β-MnO_2 and (D) R-$Fe_xMn_{1-x}O_2$ (x≈3 wt.%); (C) XRD patterns; (E) N_2 adsorption/desorption isotherms and corresponding pore size distributions (inset); (F) Fe 2p XPS spectra; (G) Surface morphology and surface quantities of the pristine surface. SEM: Scanning electron microscopy; BET: brunauer-emmett-teller; XPS: X-ray photoelectron spectrometer; SABs: spent alkaline batteries; XRD: X-ray diffraction.

[Figure 2B3][26]. The HRTEM image of R-$Fe_xMn_{1-x}O_2$ clearly shows lattice fringes of (400) (d = 0.24 nm) and (211) (d = 0.22 nm), forming an included angle of 61.8° and it can be assigned to R-MnO_2[27]. In contrast, β-MnO_2 shows lattice fringes of 0.22 nm (200) and 0.21 nm (111) with θ = 47.7° [Figure 2A]. These results were consistent with XRD patterns and confirm the structure of R-$Fe_xMn_{1-x}O_2$, which facilitates the insertion/extraction of Zn^{2+} compared to β-MnO_2. EDS analysis [Figure 2C] demonstrated the presence of C, Mn, O and Fe elements, with no detectable Zn, confirming the formation of homogeneous Fe^{3+}-doped R-$Fe_xMn_{1-x}O_2$, which regulates the lattice structure and optimizes ion diffusion.

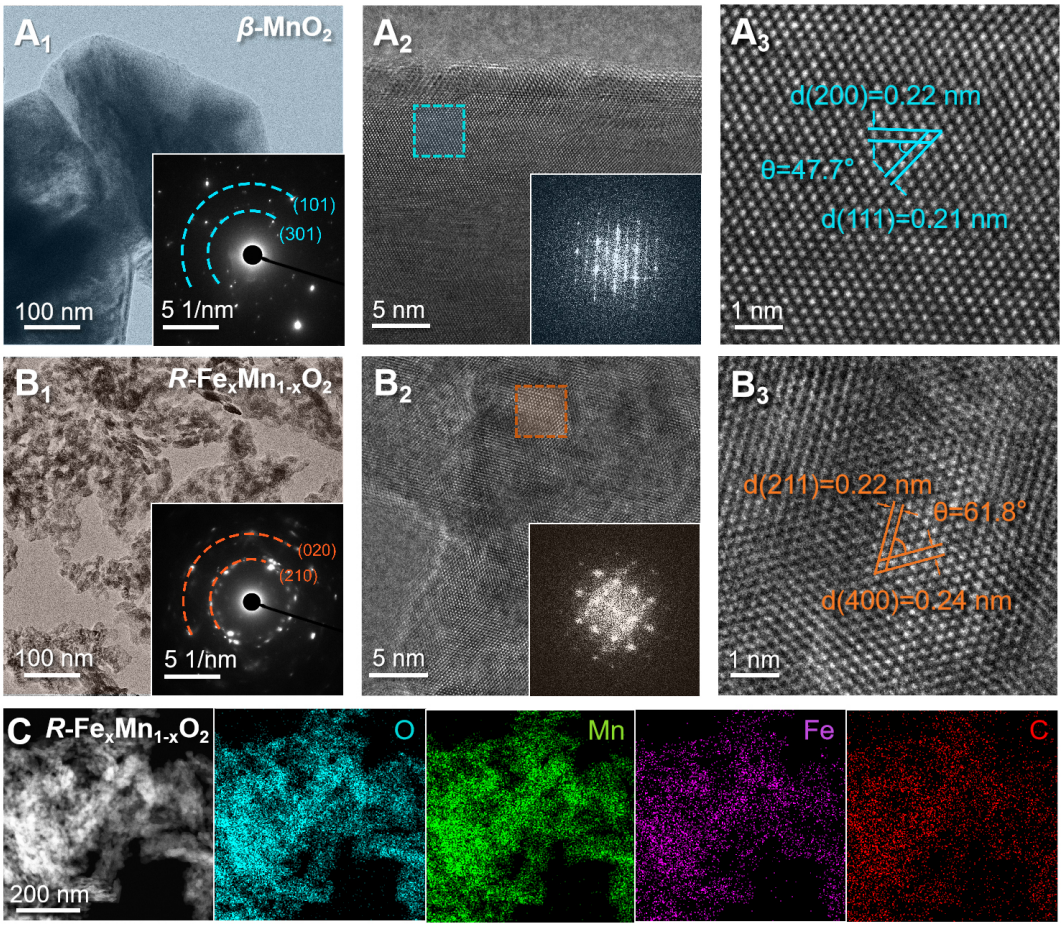


Figure 2. The TEM and HRTEM images with corresponding SAED images of (A) β-MnO_2, (B) *R*-$Fe_xMn_{1-x}O_2$. (C) corresponding elemental mapping images of *R*-$Fe_xMn_{1-x}O_2$ powders. TEM: Transmission electron microscopy; HRTEM: high-resolution transmission electron microscopy; SAED: selective area electron diffraction.

To verify the role of Fe^{3+} doping in enhancing electrode stability and reaction kinetics, we assembled coin cells to evaluate the electrochemical performance of the materials.

We systematically evaluated the effect of Fe^{3+} feeding amount on the electrode materials and found that the optimal electrochemical performance was achieved at a Mn:Fe feeding ratio of 100:5 [Supplementary Figures 9-11]. Figure 3A shows the cycling performance of the β-MnO_2 and *R*-$Fe_xMn_{1-x}O_2$ electrodes. The results demonstrate enhanced cycling stability for *R*-$Fe_xMn_{1-x}O_2$ cathodes compared to β-MnO_2 cathodes. At 1.0 A g^{-1}, the *R*-$Fe_xMn_{1-x}O_2$ cathode exhibited specific capacity of 161.9 mAh g^{-1} and achieved 88.9% capacity retention after 1000 cycles. In contrast, the β-MnO_2 cathode showed a specific capacity of 52.58 mAh g^{-1} and retained only 48.8 % after cycling [Figure 3A]. The superior cycling capability of *R*-$Fe_xMn_{1-x}O_2$ can be attributed to Fe^{3+} doping, which optimizes ion diffusion pathways and enhances the stability of Mn-O bonds (~1.91 Å) through substitution with shorter Fe-O bonds (~1.89 Å). Additionally, the *R*-$Fe_xMn_{1-x}O_2$ cathodes demonstrated much better rate performance than β-MnO_2 cathodes [Figure 3B and Supplementary Figure 11], delivering specific capacities of 286.8, 269.7, 248.5, 206.8, and 163.3mAh g^{-1} at current densities of 0.1, 0.2, 0.5, 1.0, and 1.5 A g^{-1}, respectively. The β-MnO_2 exhibited poor rate capability, achieving only 30.9 mAh g^{-1} at 1.5 A g^{-1}. Figure 3C illustrates the galvanostatic charge-discharge curve (GCD) profiles of *R*-$Fe_xMn_{1-x}O_2$ and β-MnO_2 cathodes at various current densities. Notably, as current density increased, the

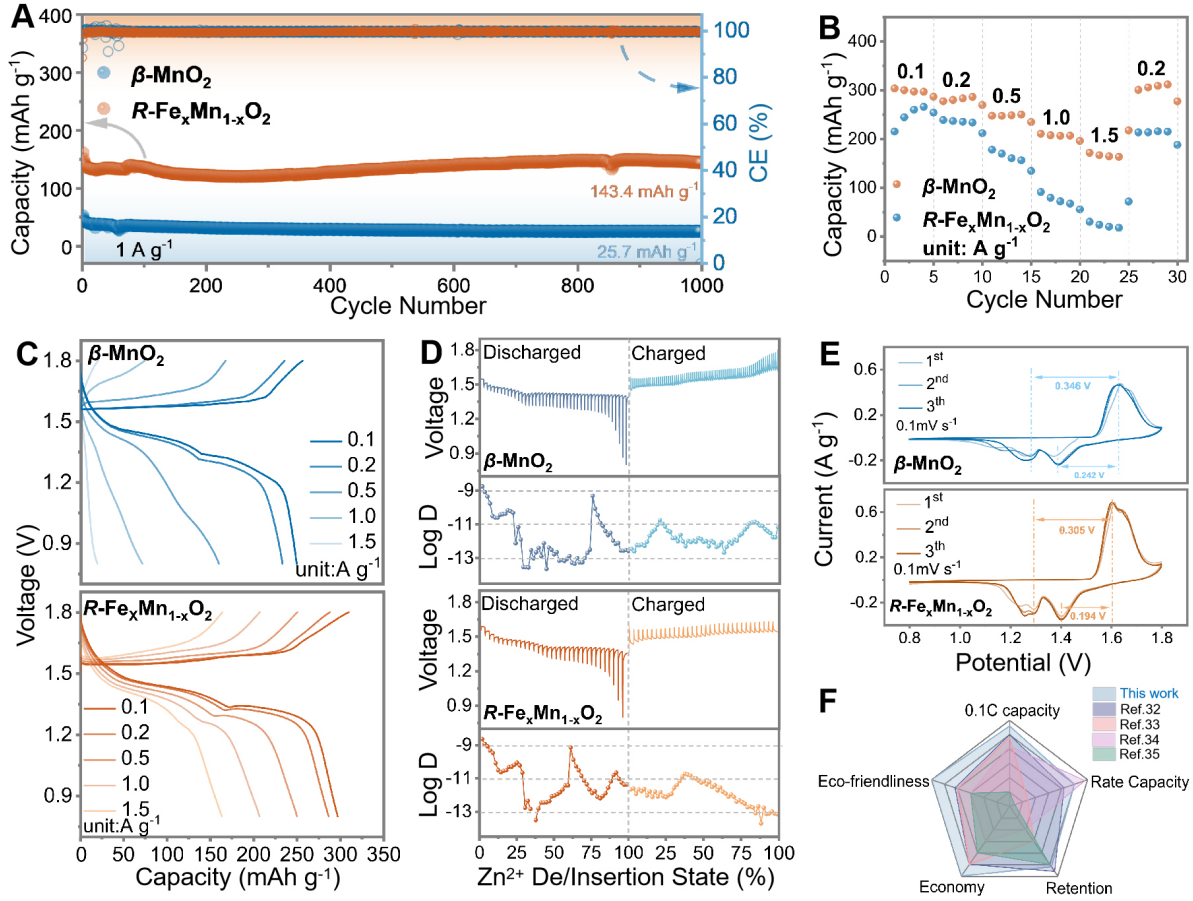


Figure 3. Electrochemical performance of β-MnO_2 and R-$Fe_xMn_{1-x}O_2$ cathodes of (A) cycling performance [Coulombic Efficiency (CE)]; (B) rate capabilities; (C) The GCD curves; (D) GITT profiles and corresponding ion diffusion coefficients of AZIBs; (E) CV curves at scan rate of 0.1 mV s^{-1}.(F) radar chart comparing properties of Mn-based cathodes for AZIBs. GCD: Galvanostatic charge-discharge; GITT: galvanostatic intermittent titration technique; AZIBs: aqueous zinc-ion batteries; CV: cyclic voltammetry.

second discharge platform below 1.3V [Figure 3C] in β-MnO_2 cathodes gradually diminished. Conversely, R-$Fe_xMn_{1-x}O_2$ maintained better plateau retention at high rates, contributing more significantly to the overall capacity.

Furthermore, Galvanostatic Intermittent Titration Technique (GITT) was employed to evaluate Zn^{2+}/H^+ diffusion kinetics. The GITT curves for β-MnO_2 and R-$Fe_xMn_{1-x}O_2$ cathodes, along with the corresponding diffusion coefficients (D) were presented in Figure 3D. The D value was calculated using $D_{Zn^{2+}} = \frac{4}{\pi\iota}(\frac{n_M V_M}{s})^2(\frac{\Delta Es}{\Delta Et})^2$. (D: diffusion coefficients; ι: the relaxation time; nM: the number of moles; VM: molar volume of the electrode material; S: the electrode/electrolyte contact area; ΔEs: the voltage change induced by the pulse; ΔEt: the voltage change during galvanostatic charge/discharge). The R-$Fe_xMn_{1-x}O_2$ cathodes exhibited significantly higher ion diffusion coefficients throughout the entire discharge process. This kinetic advantage correlates with the stabilized (1 × 2) tunnel structure and optimized cation diffusion pathways of R-$Fe_xMn_{1-x}O_2$. Besides, CV profiles at 0.1 mV s^{-1} [Figure 3E] revealed larger redox peaks for the R-$Fe_xMn_{1-x}O_2$ cathode, indicating higher electrochemical activity. More stable redox profiles demonstrated better reversibility, attributed to enhanced mechanical stability of ion transport channels by Fe^{3+} doping. The peak splitting observed in the CV curves at 1.60-1.65 V is influenced by the Zn^{2+}/H^+ co-insertion mechanism. This peak splitting originates from the energy barrier differences between H^+ and Zn^{2+}

deintercalation pathways, which leads to divergent transport kinetics and stepwise oxidation processes. In addition, the *R*-$Fe_xMn_{1-x}O_2$ showed smaller ΔE values between redox peaks, signifying superior electrochemical reversibility, reduced polarization, improved energy retention, and enhanced overall efficiency. Collectively, the cathode material obtained in this work exhibits superior overall performance [Figure 3F and Supplementary Table 1].

These findings suggest that Fe^{3+} doping stabilizes the *R*-MnO_2 structure, forming the *R*-$Fe_xMn_{1-x}O_2$ cathode, which not only alleviates lattice strain to enhance structural resilience against H^+/Zn^{2+} extraction/insertion during cycling but also accelerates reaction kinetics. To figure out the structural transitions and reversibility, *in situ* XRD analysis was performed on the *R*-$Fe_xMn_{1-x}O_2$ cathode [Supplementary Figure 12]. During discharge, new diffraction peaks emerged corresponding to $Zn_4SO_4(OH)_6{\cdot}5H_2O$ (JCPDS #039-0688), attributed to precipitation involving dissolved H^+ ions from the electrolyte. These peaks disappeared during charging. Notably, the peak intensities of *R*-MnO_2 remained basically unchanged throughout the cycling process, confirming the structural stability of *R*-$Fe_xMn_{1-x}O_2$ under electrochemical operation.

By plotting $i/v^{1/2}$ versus $v^{1/2}$ [$i(V) = k_1v^{1/2} + k_2v$] at different potentials, the values of k_1 were obtained to calculate the percentage of capacitance contribution. The capacitive contribution for the *R*-$Fe_xMn_{1-x}O_2$ electrode increased gradually from 47% to 87%, while ranging between 33% and 73% for the *β*-MnO_2 electrode [Figure 4A and Supplementary Figure 13], demonstrating the relatively higher capacitance contribution of *R*-$Fe_xMn_{1-x}O_2$ cathode[28]. Thus, the enhancement stems from the Fe^{3+}-induced porous nanostructure of *R*-$Fe_xMn_{1-x}O_2$, which increases the specific surface area and provides additional active sites for faradic reactions, thereby improving surface pseudo-capacitance. Post-cycling XPS analysis [Figure 4B and Supplementary Figure 14] revealed higher Mn^{4+} content in *R*-$Fe_xMn_{1-x}O_2$ compared to *β*-MnO_2. This effectively suppresses the Mn^{3+} proportion, mitigating Jahn-Teller distortion-induced manganese dissolution and enhancing capacity retention. The O 1s spectra showed significantly intensified H-O-H peaks in cycled *R*-$Fe_xMn_{1-x}O_2$, indicating guest-bonded water that provides shielding by reducing positive charge density at vertex oxygen sites within the host frameworks[29]. Based on above, Fe^{3+} provided more active sites and expedited reaction kinetics.

EIS before and after 1000 cycles (at 1 A g^{-1}) further elucidated the role of Fe doping in enhancing interfacial stability, as shown in Figure 4C-E. Due to abundant electrochemically active sites and accelerated ion diffusion kinetics, the charge transfer resistance (R_{ct}) value after cycling was significantly lower for *R*-$Fe_xMn_{1-x}O_2$ (562.9Ω) than for *β*-MnO_2 (1,720 Ω) [Supplementary Table 2][30]. EIS analysis during cycling stages revealed larger semicircles for both cathodes during charging and post-cycling, correlating with degradation mechanisms. However, *R*-$Fe_xMn_{1-x}O_2$ maintained more favorable reaction kinetics[31,32]. The SEM images confirmed significantly more dissolution in *β*-MnO_2 than in R-$Fe_xMn_{1-x}O_2$, consistent with the performance degradation mechanisms in Mn-based cathodes. The dissolution of Mn-based materials reduced surface active sites, impaired ion diffusion driving force, and increased R_{ct}, leading to elevated impedance and irregular morphologies [Figure 4F][33-35]. This post-cycle analysis highlights how Fe^{3+} doping in manganese-based cathodes effectively mitigates the capacity fading inherent to manganese oxide cathodes in AZIBs.

CONCLUSIONS

Fe^{3+} doping fundamentally transforms the structural stability and electrochemical behavior of metastable ramsdellite MnO_2 for zinc-ion batteries. By introducing Fe^{3+} during the hydrothermal conversion of spent $ZnMn_2O_4$, we achieve R-$Fe_xMn_{1-x}O_2$ with engineered (1 × 2) tunnels, reduced surface energy, and optimized Mn^{4+}/Mn^{3+} ratios. The Fe-mediated mechanism suppresses phase transition to *β*-MnO_2, alleviates lattice

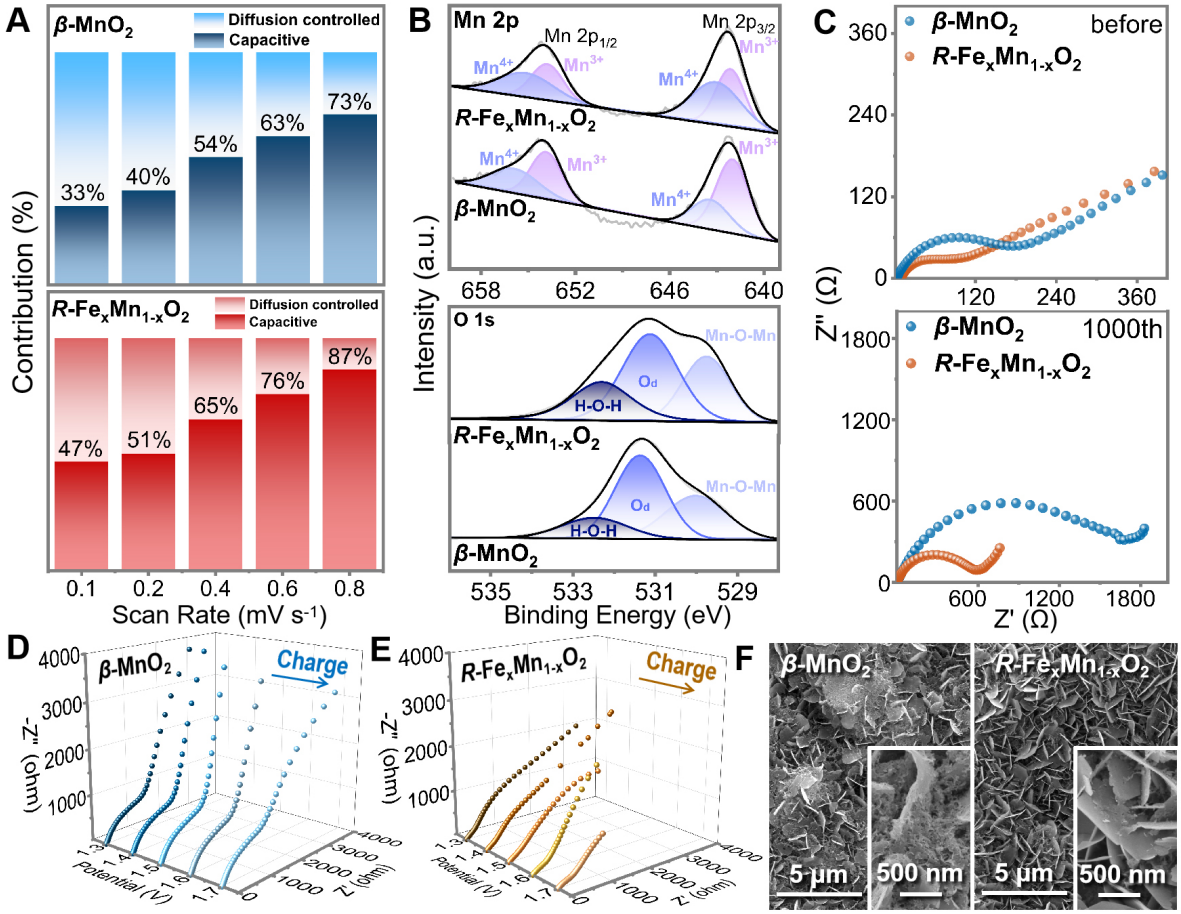


Figure 4. Capacitive behaviors and both electrochemical and morphological analysis after 1000 cycles of β-MnO_2 and R-$Fe_xMn_{1-x}O_2$ cathodes: (A) Diffusion-controlled and surface-controlled contributions to capacity at different scan rates; (B) Mn 2p and O 1s spectra; (C) Nyquist plots at the open circuit voltage state (Supplementary Figure 15 illustrates the electrical equivalent circuit used for fitting EIS spectra); (D and E) EIS spectra of β-MnO_2 and R-$Fe_xMn_{1-x}O_2$ cathodes during charge process; (F) SEM images of β-MnO_2 and R-$Fe_xMn_{1-x}O_2$ cathodes. EIS: Electrochemical impedance spectroscopy; SEM: scanning electron microscopy.

strain, and enhances Zn^{2+}/H^+ diffusion kinetics, validated by DFT calculations showing lowered surface energy and EIS revealing reduced charge-transfer resistance. Consequently, R-$Fe_xMn_{1-x}O_2$ delivers a high capacity of 286.8 mAh g^{-1} at 0.1 A g^{-1}, exceptional rate capability (163.3 mAh g^{-1} at 1.5 A g^{-1}), and long-term stability (88.9% capacity retention after 1000 cycles). Post-cycling analyses confirm Fe^{3+} mitigates Mn dissolution and structural degradation. This study highlights Fe^{3+} doping as a universal tunnel-engineering strategy to unlock the potential of metastable MnO_2 phases, while offering a sustainable route to repurpose battery waste into high-performance cathodes.

DECLARATIONS

Authors' contributions

Data curation, methodology, software, writing - original draft, writing - review and editing, funding acquisition: Meng, Y.

Investigation, software, writing - review and editing: Li, Y.

Investigation, software: Xiao, H.; Wang, Z.

Investigation, writing-review and editing: Wang, X.

Software, resources, writing - review and editing: Zhang, F.
Investigation, software, writing - review and editing: Ma, W.
Resources: Xiong, D.; Zhou, T.; Yin, J.
Writing-review and editing: Xiao, Z.
Resources, funding acquisition: Yuan, Z.
Conceptualization, formal analysis, funding acquisition, methodology, resources, supervision, writing-review and editing: Yang, L.
Data analysis, resources: Liu, C.
Supervision, resources: Wu, X.

Availability of data and materials

The linked data has been added to the manuscript. The raw/ processed data required to reproduce these findings can be obtained upon request from the first author.

Financial support and sponsorship

This work is supported by Natural Science Foundation of China (52234001), Science and Technology Planning Project of Hunan Province (2018TP1017), and National Students' Platform for Innovation and Entrepreneurship Training Program (S202410542060).

Conflicts of interest

Wu, X. is Editorial Board Member of the journal *Energy Materials*. Wu, X. was not involved in any steps of editorial processing, notably including reviewers' selection, manuscript handling, and decision making. Yuan, Z. and Zhou, T. are affiliated with Xiangtan Electrochemical Technology Co., Ltd. The other authors declare that there are no conflicts of interest.

Ethical approval and consent to participate

Not applicable.

Consent for publication

Not applicable.

Copyright

© The Author(s) 2025.

REFERENCES

1. Chao, D.; Zhou, W.; Xie, F.; et al. Roadmap for advanced aqueous batteries: From design of materials to applications. *Sci. Adv.* **2020**, *6*, eaba4098. DOI PubMed PMC
2. Lai, G.; Zhao, Z.; Zhang, H.; et al. In-situ positive electrode-electrolyte interphase construction enables stable Ah-level Zn-MnO_2 batteries. *Nat. Commun.* **2025**, *16*, 2194. DOI PubMed PMC
3. Luo, C.; Lei, H.; Xiao, Y.; et al. Recent development in addressing challenges and implementing strategies for manganese dioxide cathodes in aqueous zinc ion batteries. *Energy. Mater.* **2024**, *4*, 400036. DOI
4. Hu, X.; Robles, A.; Vikström, T.; Väänänen, P.; Zackrisson, M.; Ye, G. A novel process on the recovery of zinc and manganese from spent alkaline and zinc-carbon batteries. *J. Hazard. Mater.* **2021**, *411*, 124928. DOI
5. Xu, Z.; Zhang, N.; Wang, X. Upcycling spent alkaline batteries into rechargeable zinc metal batteries. *Nano. Energy.* **2022**, *102*, 107724. DOI
6. Zhu, J.; Tie, Z.; Bi, S.; Niu, Z. Towards more sustainable aqueous zinc-ion batteries. *Angew. Chem. Int. Ed.* **2024**, *63*, e202403712. DOI PubMed
7. Kitchaev, D. A.; Dacek, S. T.; Sun, W.; Ceder, G. Thermodynamics of phase selection in MnO_2 framework structures through alkali intercalation and hydration. *J. Am. Chem. Soc.* **2017**, *139*, 2672-81. DOI PubMed
8. Peng, H.; Wang, C.; Wang, D.; Song, X.; Zhang, C.; Yang, J. Dynamic Zn/electrolyte interphase and enhanced cation transfer of sol electrolyte for all-climate aqueous zinc metal batteries. *Angew. Chem. Int. Ed.* **2023**, *62*, e202308068. DOI

9. Abdalla, K. K.; Wang, Y.; Abdalla, K. K.; et al. Rational design and prospects for advanced aqueous Zn-organic batteries enabled by multielectron redox reactions. *Sci. China. Mater.* **2024**, *67*, 1367-78. DOI
10. Xiao, H.; Xiong, D.; Lu, B.; et al. Ramsdellite-MnO_2 regeneration via acid-mediated redox tuning toward rechargeable aqueous zinc-ion batteries. *Inorg. Chem.* **2025**, *64*, 8322-33. DOI
11. Cao, J. M.; Liu, Y.; Li, K.; et al. Coulombic-hinderance regulation on pyrovanadates for practicable calcium-ion batteries: a solid-solution strategy. *Natl. Sci. Rev.* **2025**, *12*, nwaf074. DOI PubMed PMC
12. Xiao, J.; Gao, H.; Xiao, Y.; et al. A hydro-stable and phase-transition-free P2-type cathode with superior cycling stability for high-voltage sodium-ion batteries. *Chem. Eng. J.* **2025**, *506*, 160010. DOI
13. Zhang, A.; Zhao, R.; Wang, Y.; et al. Hybrid superlattice-triggered selective proton grotthuss intercalation in δ-MnO_2 for high-performance zinc-ion battery. *Angew. Chem. Int. Ed.* **2023**, *62*, e202313163. DOI
14. Huang, X.; Li, Y.; Yan, X.; et al. Microstructure optimization and electrochemical behavior of in-situ growth Ramsdellite-MnO_2@NCA-LDH@CC for supercapacitors and oxygen evolution reaction catalysts. *J. Materiomics.* **2024**, *10*, 552-65. DOI
15. Chen, C.; Xu, K.; Ji, X.; Zhang, B.; Miao, L.; Jiang, J. Enhanced electrochemical performance by facile oxygen vacancies from lower valence-state doping for ramsdellite-MnO_2. *J. Mater. Chem. A.* **2015**, *3*, 12461-7. DOI
16. Li, S.; Zhong, Y.; Huang, J.; et al. Regulating interfacial kinetics boosts the durable A h-level zinc-ion batteries. *Energy. Environ. Sci.* **2025**, *18*, 2599-609. DOI
17. Li, X.; Yu, J.; Low, J.; Fang, Y.; Xiao, J.; Chen, X. Engineering heterogeneous semiconductors for solar water splitting. *J. Mater. Chem. A.* **2015**, *3*, 2485-534. DOI
18. Xu, Y.; Wang, Y.; Dong, N.; et al. Novel polyimide binder for achieving high-rate capability and long-term cycling stability of $LiNi_{0.8}Co_{0.1}Mn_{0.1}O_2$ cathode via constructing polar and micro-branched crosslinking network structure. *J. Energy. Chem.* **2023**, *76*, 19-31. DOI
19. Pan, G.; Wang, Z.; Zhang, J.; Cao, M.; Zhang, L.; Zhang, J. Porous carbon-coated Fe-doped MnO as high-performance cathode for aqueous zinc ion batteries. *Energy. Tech.* **2025**, *13*, 2401690. DOI
20. Zhong, Z.; Li, J.; Li, L.; et al. Improving performance of zinc-manganese battery via efficient deposition/dissolution chemistry. *Energy. Storage. Mater.* **2022**, *46*, 165-74. DOI
21. Yang, Z.; Pan, X.; Shen, Y.; et al. New insights into phase-mechanism relationship of Mg_xMnO_2 nanowires in aqueous zinc-ion batteries. *Small* **2022**, *18*, 2107743. DOI
22. Li, X.; Sun, Y.; Zhou, L.; et al. Suppressing Jahn-Teller distortion and locking lattice water with doped Fe(III) in birnessite toward fast and stable zinc-ion batteries. *Mater. Horiz.* **2024**, *11*, 4133-43. DOI
23. Chen, X.; Han, L.; Zhao, G.; et al. Construction of MnO_2-Mn_3O_4 heterostructures to facilitate high-performance aqueous magnesium ion energy storage. *Chem. Commun.* **2024**, *60*, 3067-70. DOI
24. Li, Z.; Huang, Y.; Zhang, J.; Jin, S.; Zhang, S.; Zhou, H. One-step synthesis of MnO_x/PPy nanocomposite as a high-performance cathode for a rechargeable zinc-ion battery and insight into its energy storage mechanism. *Nanoscale* **2020**, *12*, 4150-8. DOI
25. Zhao, Y.; Zhang, S.; Zhang, Y.; et al. Vacancy-rich Al-doped MnO_2 cathodes break the trade-off between kinetics and stability for high-performance aqueous Zn-ion batteries. *Energy. Environ. Sci.* **2024**, *17*, 1279-90. DOI
26. Ding, S.; Zhang, M.; Qin, R.; et al. Oxygen-deficient β-MnO_2@ graphene oxide cathode for high-rate and long-life aqueous zinc ion batteries. *Nano-Micro. Lett.* **2021**, *13*, 173. DOI
27. Yang, X.; Qiao, Z.; Liu, F.; et al. In-depth study of electrochemical capacitor performance of MnO_2 during phase transition from Ramsdellite-MnO_2 to birnessite-MnO_2. *Electrochim. Acta.* **2018**, *280*, 77-85. DOI
28. Huang, H.; Feng, H.; He, Z.; et al. Enhancing Zn^{2+}/H^+ joint charge storage in MnO_2: concurrently tailoring Mn's local electron density and O's p-band center. *ACS. Nano.* **2024**, *18*, 25601-13. DOI
29. Yao, H.; Yu, H.; Zheng, Y.; et al. Pre-intercalation of ammonium ions in layered δ-MnO_2 nanosheets for high-performance aqueous zinc-ion batteries. *Angew. Chem. Int. Ed.* **2023**, *62*, e202315257. DOI
30. Xu, Z.; Wang, J.; Zhang, W.; et al. Hydrogen-bond chemistry inhibits Jahn-Teller distortion caused by Mn 3d orbitals for long-lifespan aqueous Zn//MnO_2 batteries. *J. Mater. Chem. A.* **2024**, *12*, 25491-503. DOI
31. Long, J.; Yang, F.; Cuan, J.; et al. BoosteD CHARGE TRANSFER IN TWINBORn α-(Mn_2O_3-MnO_2) heterostructures: toward high-rate and ultralong-life zinc-ion batteries. *ACS. Appl. Mater. Interfaces.* **2020**, *12*, 32526-35. DOI
32. Jiang, S.; Han, W.; Fang, L.; et al. Achieving non-interfacial blocking zinc ion transport based on MOF derived manganese oxides and amorphous carbon hybrid materials. *Chem. Eur. J.* **2024**, *30*, e202401802. DOI
33. Ren, Y.; Meng, F.; Zhang, S.; et al. CNT@MnO_2 composite ink toward a flexible 3D printed micro-zinc-ion battery. *Carbon. Energy.* **2022**, *4*, 446-57. DOI
34. Ruo, H.; Chen, L.; Huang, J.; et al. Constructing low-cost stable zinc-ion batteries with sodium-rich monoclinic manganese hexacyanoferrate cathode. *Surf. Interfaces.* **2024**, *51*, 104594. DOI
35. Zhang, Y.; Lin, X.; Tang, X.; et al. Ultrathin polyaniline-coated single-crystalline Mn_2O_3 nanoporous ellipsoids with high energy density and cyclability for low-cost zinc-ion batteries. *ACS. Appl. Nano. Mater.* **2022**, *5*, 12729-36. DOI